Submitted to ApJS 2019 Jul 14; Accepted 2019 Dec 4
Preprint typeset using LaTeX style emulateapj v. 12/16/11

HST/COS OBSERVATIONS OF QUASAR OUTFLOWS IN THE 500 – 1050 Å REST FRAME: VI WIDE, ENERGETIC OUTFLOWS IN SDSS J0755+2306

Xinfeng Xu[1,†], Nahum Arav[1], Timothy Miller[1], Gerard A. Kriss[2], Rachel Plesha[2]
[1]Department of Physics, Virginia Tech, Blacksburg, VA 24061, USA
[2]Space Telescope Science Institute, 3700 San Martin Drive, Baltimore, MD 21218, USA

Submitted to ApJS 2019 Jul 14; Accepted 2019 Dec 4

ABSTRACT

We present the analysis of two outflows (S1 at –5500 km s^{-1} and S2 at –9700 km s^{-1}) seen in recent HST/COS observations of quasar SDSS J0755+2306 (z = 0.854). The outflows are detected as absorption troughs from both high-ionization species, including N III, O III, and S IV, and very high-ionization species, including Ar VIII, Ne VIII, and Na IX. The derived photoionization solutions show that each outflow requires a two ionization-phase solution. For S1, troughs from S IV* and S IV allow us to derive an electron number density, $n_e = 1.8\times10^4$ cm^{-3}, and its distance from the central source of $R = 270$ pc. For S2, troughs from O III* and O III yield $n_e = 1.2\times10^3$ cm^{-3} and $R = 1600$ pc. The kinetic luminosity of S2 is > 12% of the Eddington luminosity for the quasar and therefore can provide strong AGN feedback effects. Comparison of absorption troughs from O III and O VI in both outflow systems supports the idea that for a given element, higher ionization ions have larger covering fractions than lower ionization ones.

Keywords: galaxies: active – galaxies: kinematics and dynamics – quasars: jets and outflows – quasars: absorption lines – quasars: general – quasars: individual (SDSS J0755+2306)

1. INTRODUCTION

Broad absorption line (BAL) outflows are detected as blueshifted absorption troughs in 15 – 25 % of quasar spectra (Tolea et al. 2002; Hewett & Foltz 2003; Reichard et al. 2003; Trump et al. 2006; Ganguly & Brotherton 2008; Gibson et al. 2009, and references therein). These outflows provide an important mechanism to carry energy, mass, and momentum out of the quasar's central regions (e.g., Scannapieco & Oh 2004; Ciotti, Ostriker & Proga 2009; Ostriker et al. 2010; Hopkins & Elvis 2010; Choi et al. 2014; Hopkins et al. 2016). Theoretical studies and simulations show that these outflows are related to a variety of AGN feedback processes (see elaboration in section 1 of Arav et al. 2019, hereafter, Paper I). To quantify the extent that outflows can contribute to AGN feedback, we need to determine their kinetic luminosity ($\dot{E}_k$). Theoretical models predict that $\dot{E}_k$ needs to be at least 0.5 % (Hopkins & Elvis 2010) or 5 % (Scannapieco & Oh 2004) of the Eddington luminosity (L_{edd}) in order to provide strong AGN feedback.

In this paper, we analyze two outflows emanating from quasar SDSS J0755+2306. The data is from a spectroscopic survey of ten quasars in the 500 – 1050 Å Extreme-UV (EUV500) band (see Paper I). These two outflows present features different from other quasar outflows observed in the EUV500: 1) deep absorption troughs from doubly ionized species, e.g., C III λ977.02 Å, the N III multiplets near 686 Å, 764 Å, and 990 Å, and the O III multiplets near 703 Å and 834 Å; 2) continuous blended absorption that depress the flux in the 1227 Å $< \lambda <$ 1290 Å and 1340 Å $< \lambda <$ 1440 Å observed frame regions.

This paper is part of a series of publications describing the results of HST program GO-14777, which observed quasar outflows in the EUV500 using the Cosmic Origin Spectrograph (COS).
Paper I (Arav et al. 2020) summarizes the results for the individual objects and discusses their importance to various aspects of quasar outflow research.
Paper II (Xu et al. 2020a) gives the full analysis for 4 outflows detected in SDSS J1042+1646, including the largest kinetic luminosity ($\dot{E}_k = 10^{47}$ erg s^{-1}) outflow measured to date at $R = 800$ pc, and an outflow at $R = 15$ pc.
Paper III (Miller et al. 2020a) analyzes 4 outflows detected in 2MASS J1051+1247, which show remarkable similarities, are situated at $R \sim 200$ pc and have a combined $\dot{E}_k = 10^{46}$ erg s^{-1}.
Paper IV (Xu et al. 2020b) presents the largest velocity shift and acceleration measured to date in a BAL outflow.
Paper V (Miller et al. 2020b) analyzes 2 outflows detected in PKS 0352-0711, one outflow at $R = 500$ pc and a second outflow at $R = 10$ pc that shows an ionization-potential-dependent velocity shift for troughs from different ions.
Paper VI is this work.
Paper VII (Miller et al. 2020c) discusses the other objects observed by program GO-14777, whose outflow characteristics make the analysis more challenging.

The structure of this paper is as follows. We present the observations and data reduction in section 2. In section 3, we present the analysis of the spectrum for the two outflow systems. We determine each outflow' electron number density (n_e) and distance in section 4 and constrain their energetics in section 5. We discuss the results and compare with other EUV500 outflows in sec-

† Email: xinfeng@vt.edu

Table 1
HST/COS Observations for SDSS J0755+2306

Epoch	Date	Exp.[1]	Grating	λ_c^2
1	2017 Sep 18	1220	G130M	1291
2	2017 Sep 18	2330	G130M	1327
3	2017 Sep 19	2330	G160M	1577
4	2017 Sep 19	2330	G160M	1600
5	2010 Dec 20	900	G140L	1280

Note. —
[1]: The exposure time of each observation in seconds.
[2]: The central wavelength of each grating in Å.

tion 6; and summarize the paper in section 7. We adopt a cosmology with $H_0 = 69.6$ km s^{-1} Mpc^{-1}, $\Omega_m = 0.286$, and $\Omega_\Lambda = 0.714$, and we use Ned Wright's Javascript Cosmology Calculator website (Wright 2006).

2. OBSERVATIONS AND DATA REDUCTION

SDSS J0755+2306 (J2000: R.A. = 07:55:14.58, decl. = +23:06:07.13, z = 0.854) was observed by HST/COS (Green et al. 2012) using gratings G130M and G160M in September of 2017 as part of our HST/COS program GO-14777 (PI: Arav). This object was observed previously in December of 2010 using the HST/COS G140L grating in the program GO-12289 (PI: J. Howk). The details of these observations are shown in table 1. We reduce and process the data and errors in the same way as described in Miller et al. (2018). We corrected for Galactic extinction with E(B-V) = 0.045 (Schlafly & Finkbeiner 2011). For the 2017 observations, we combined the two observations for each grating to increase the signal to noise. We show the full, dereddened spectrum in figure 1. For regions outside the wavelength range of the 2017 epoch data, we show the 2010 epoch data.

Two outflow systems are identified: S1 has a velocity centroid (v_c) at –5520 km s^{-1} (based on its S IV λ809.66 trough) and S2 at –9660 km s^{-1} (based on its S VI λ933.38 trough). In figure 1, absorption troughs associated with S1 and S2 are shaded in red and blue, respectively. Blended regions of the two outflow systems are shaded green. The unabsorbed emission model is comprised of a power law continuum and strong emission lines fitted with Gaussian profiles (Chamberlain et al. 2015; Miller et al. 2018; Xu et al. 2018). The Galactic damped Lyα absorption is modeled with a Voigt profile ($\log(N_H) = 20.4^{+0.15}_{-0.15}$ cm^{-2}, e.g., Prochaska et al. 2005). The final, adopted emission model is shown as the solid red line in figure 1.

3. SPECTRAL ANALYSIS

3.1. *Column Density Determinations*

The ionic column densities ($N_{\rm ion}$) measured from the spectra represent the ionization structure of the observed outflow material. Like in all 11 outflows in the other objects (see table 1 of Paper I), we observe in S1 and S2 strong absorption troughs from very high-ionization species, including Ar VIII, Ne VIII, Na IX, and Mg X. Similar to 10 of the outflows in the other objects (the exception is S4 of SDSS J1042+1646, see Paper IV), we observe in S1 and S2 absorption troughs from triply ionized species, e.g., N IV, O IV, and S IV. We also observe

Table 2
Ionic Column Densities for Outflows in SDSS J0755+2306

Ion	$\lambda^{(1)}$ (Å)	$N_{ion,mea}{}^{(2)}$ $\log(\mathrm{cm}^{-2})$	$\frac{N_{ion,mea}}{N_{ion,model}}{}^{(3)}$
Outflow S1, v = [-7000, -5200][(4)]			
H I	949.74	<15.96	<0.85
N III	685.52	>15.55	>1.12
O III	832.93	>16.02	>1.20
O V	630.80	>15.83	>0.12
O VI	1037.62	>16.30	>0.24
Ne VIII	780.32	>16.49	>1.00
Na IX	682.72	<15.71	<31.6
Mg X	624.94	>16.69	–[5]
S IV+S IV*	809.66, 815.94	$15.32^{+0.12}_{-0.16}$	0.85
S VI	944.52	>15.56	>1.12
Ar IV	850.60	<14.78	<1.51
Ar VIII	713.80	<15.14	<3.80
Ca VII	624.38	>15.40	–[5]
Outflow S2, v = [-11200, 8000][(4)]			
H I	972.54	<16.15	<1.02
H I	1025.72	>15.68	>0.35
N III	685.52	>15.63	>1.23
O III	832.93	>15.76	>1.12
O V	630.80	>15.98	>0.06
O VI	1037.62	>16.49	>0.05
Ne VIII	770.41	>16.47	>0.31
Na IX	682.72	<15.40	<7.24
Mg X	624.94	>16.40	–[5]
S IV+S IV*	809.66, 815.94	<15.37	<1.35
S VI	933.38	>15.59	>1.12
Ar IV	850.60	<14.68	<1.78
Ar VIII	700.24	>15.39	>0.41
Ca VII	624.38	>15.70	–[5]

Note. —
[1] The rest wavelength of the measured transitions for each ion. For ions which are a doublet or multiplet, we show all the uncontaminated transitions.
[2] The measured $N_{\rm ion}$. Lower limits are shown in blue while upper limits are shown in red. S IV+S IV* is for the sum of the resonance and excited transitions for S IV.
[3] The ratio of the measured $N_{\rm ion}$ to the model predicted $N_{\rm ion}$.
[4] The N_{ion} integration range in km s^{-1}.
[5] For the transitions of Mg X λ624.94 and Ca VII λ624.38, their absorption troughs are too close to be disentangled. We report the $N_{\rm ion}$ values for Mg X or Ca VII assuming that the whole blended trough is from Mg X or Ca VII, respectively (see section 3.1). In the photoionization models, we investigated several possible scenarios (section 3.2).

absorption troughs from doubly ionized species in S1 and S2, including C III, N III, and O III. The only other outflow analyzed in our EUV500 program that shows such troughs is the –3150 km s^{-1} outflow system in Paper V. Overall, we observe troughs in quasar SDSS J0755+2306 from ions with a larger spread of ionization potentials (48 eV $\sim$ 367 eV) than in most of the other analyzed outflows in our EUV500 program. The atomic data for these transitions are shown in table 3 of Paper II.

Following the methodology in section 3 of Paper II, we analyze the data and measure $N_{\rm ion}$ as follows. Most measured $N_{\rm ion}$ use the apparent optical depth (AOD) method. Visual inspection of the troughs between epochs show no significant variability. Therefore, when possible, we use the $N_{\rm ion}$ measurements from the 2017 epoch data since it has higher signal-to-noise and spectral resolution. Most of the measured troughs are treated as lower limits since their levels of non-black saturation are un-

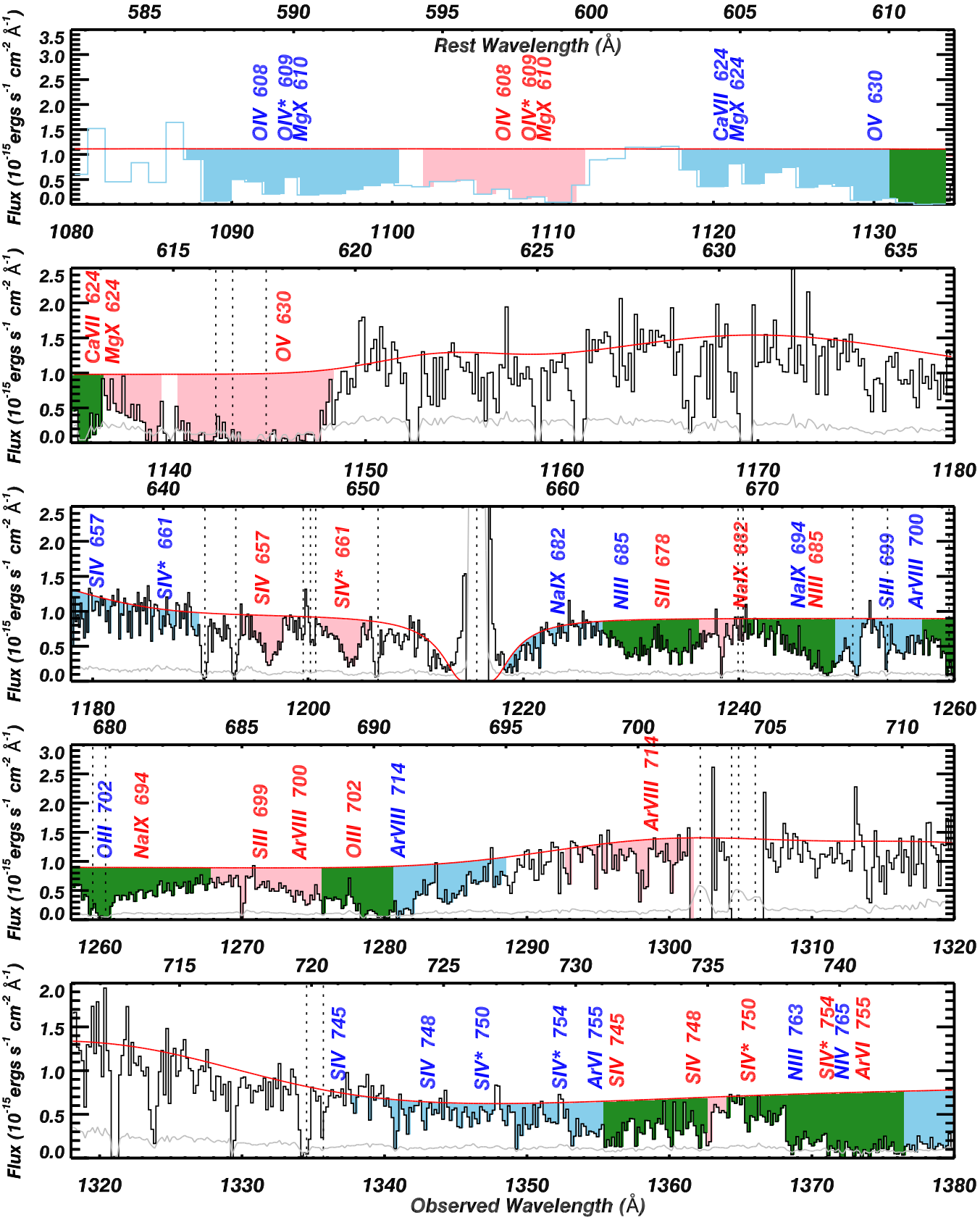

Figure 1. HST/COS dereddened spectrum of SDSS J0755+2306 (z = 0.854). The black histogram shows the data from the 2017 epoch. The unabsorbed emission model and the flux error are shown as the red and gray solid lines, respectively. We shade the significant ionic absorption troughs for the two outflow systems, S1 and S2, of the 2017 epoch in red and blue, respectively. Blended regions of the two outflow systems are shaded green. Strong Galactic interstellar medium (ISM) lines (e.g., C II λ1334.53 and C II* λ1335.71) and geocoronal lines (e.g., H I at 1215.67 Å, O I at 1302.17 Å, and O I* at 1304.86 Å, 1306.03 Å) are marked with black dotted lines. The Galactic damped Lyα (at 1215.67 Å rest frame) is modeled by a Voigt profile with $\log(N_{\rm H}) = 20.4$ cm^{-2}. The 2010 data are the blue histograms in the first panel. This covers an extra wavelength range from 1080 – 1135 Å. The 2010 data are consistent with the 2017 data in the overlapping regions.

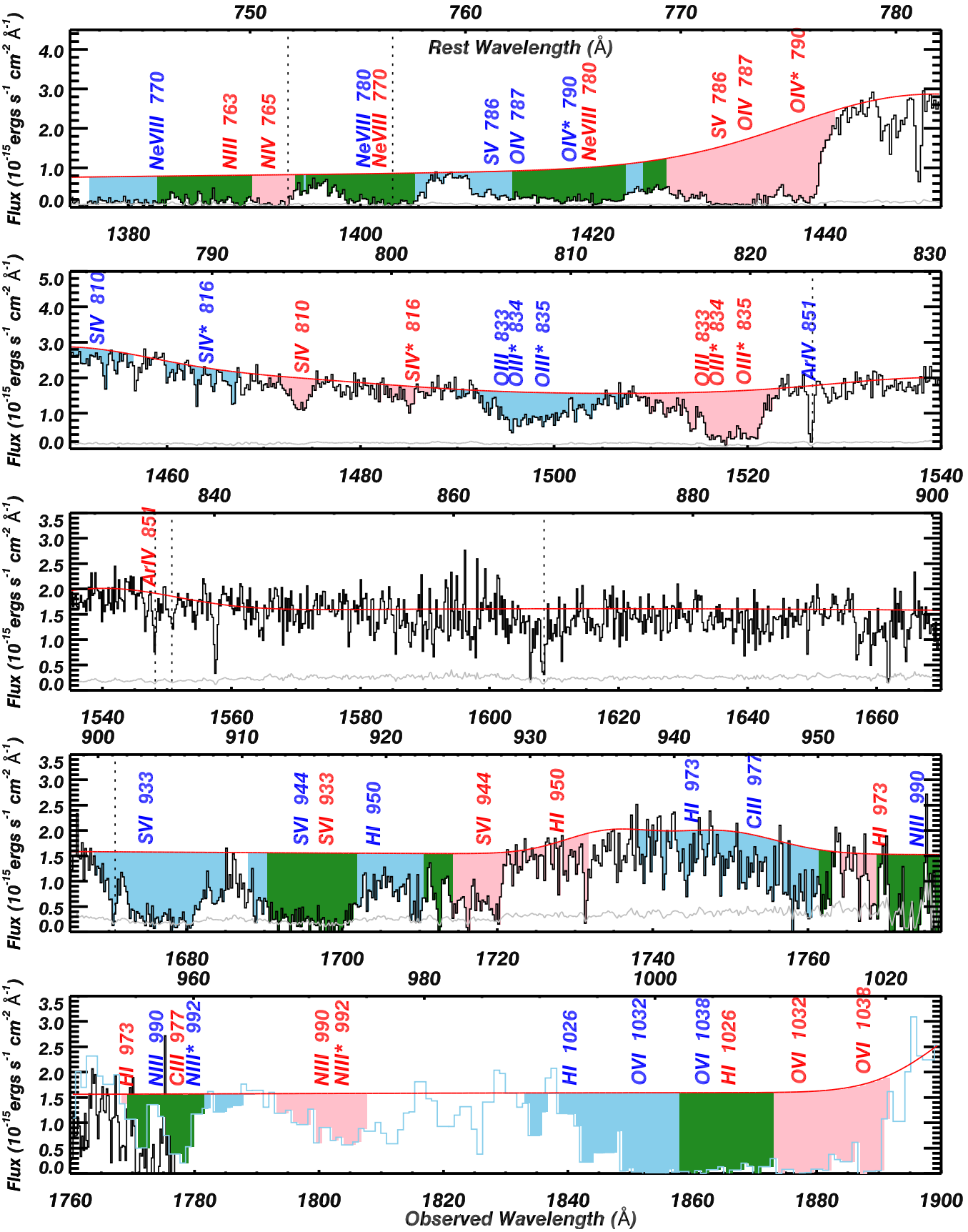

Figure 1 (Continued). The 2010 data are the blue histograms in the last panel. This covers an extra wavelength range from 1778 – 1900 Å. The 2010 data are consistent with the 2017 data in the overlapping regions.

known without available partial covering (PC) solutions (Borguet et al. 2012b). For absorption trough regions with a maximum optical depth, $\tau_{max} < 0.05$, we consider their AOD $N_{\rm ion}$ as upper limits. In section 4, we show that we can obtain $N_{\rm ion}$ measurements for S IV and S IV* for S1. We show the measured $N_{\rm ion}$ in the third column of table 2 and the corresponding ion and wavelength in the first two columns. All troughs in figure 1 that are not listed in table 2 are severely blended, yielding unreliable $N_{\rm ion}$ measurements or limits.

For the transitions of Mg X λ624.94 and Ca VII λ624.38, their absorption troughs are too close to be disentangled (S1 around 1135 Å and S2 around 1120 Å, observed-frame). In table 2, we report the $N_{\rm ion}$ values for Mg X or Ca VII assuming that the whole blended trough is from Mg X or Ca VII, respectively. When determining the photoionization solutions, we investigate several possible scenarios for the blending between Mg X and Ca VII (see section 3.2).

For the $N_{\rm ion}$ of H I in S2, the ionic transition of H I λ972.54 does not show consistently deep absorption trough features near 1745 Å observed-frame. Therefore, we measure the AOD $N_{\rm ion}$ from the trough of H I λ972.54 and treat it as an upper limit for H I. The ionic transition of H I λ1025.72 exhibits deep absorption near 1840 – 1845 Å observed-frame, while the right wing is blended with O VI λ1031.91. We assume the trough from H I λ1025.72 is symmetric and double its blue half AOD value for the lower limit $N_{\rm ion}$ of H I. Therefore, the $N_{\rm ion}$ of H I for outflow S1 is constrained to the range of 15.68 to 16.15 [in units of log(cm^{-2})].

3.2. *Photoionization Analysis*

We assume the spectral energy distribution HE0238 SED (Arav et al. 2013). This SED is physically plausible since it is based on observations of quasar HE 0238–1904 in the EUV500 band (Arav et al. 2013). Two main parameters govern the photoionization structure of each outflow: the total hydrogen column density ($N_{\rm H}$) and the ionization parameter ($U_{\rm H}$):

$$U_{\rm H} \equiv \frac{Q_{\rm H}}{4\pi R^2 n_{\rm H} c} \qquad (1)$$

where R is the distance from the central source to the absorber, $n_{\rm H}$ is the hydrogen number density, c is the speed of light, and $Q_{\rm H} = 3.1 \times 10^{56}$ s^{-1} is the emission rate of hydrogen-ionizing photons (obtained by integrating the HE0238 SED for energies above 1 Ryd). The corresponding bolometric luminosity is $\sim 4.4 \times 10^{46}$ erg s^{-1}.

We start with assuming solar metallicity and compare the measured N$_{ion}$ (table 2) to the model predicted N$_{ion}$ from the spectra synthesis code Cloudy [version c17.00, Ferland et al. (2017)] (top panel of figure 2). The colored contours for individual ions show where the measured N$_{ion}$ are consistent ($\leq 1\sigma$) with the modelled N$_{ion}$ from Cloudy (Borguet et al. 2012a). The colored contours with solid lines are N$_{ion}$ measurements, and dotted or dashed lines are N$_{ion}$ upper or lower limits, respectively. It is evident that there is no viable solution for solar metallicity. Any solution that matches the upper limit N$_{ion}$ of H I will simultaneously underpredict N$_{ion}$ of N III, S IV, and S VI by up to a factor of 5.

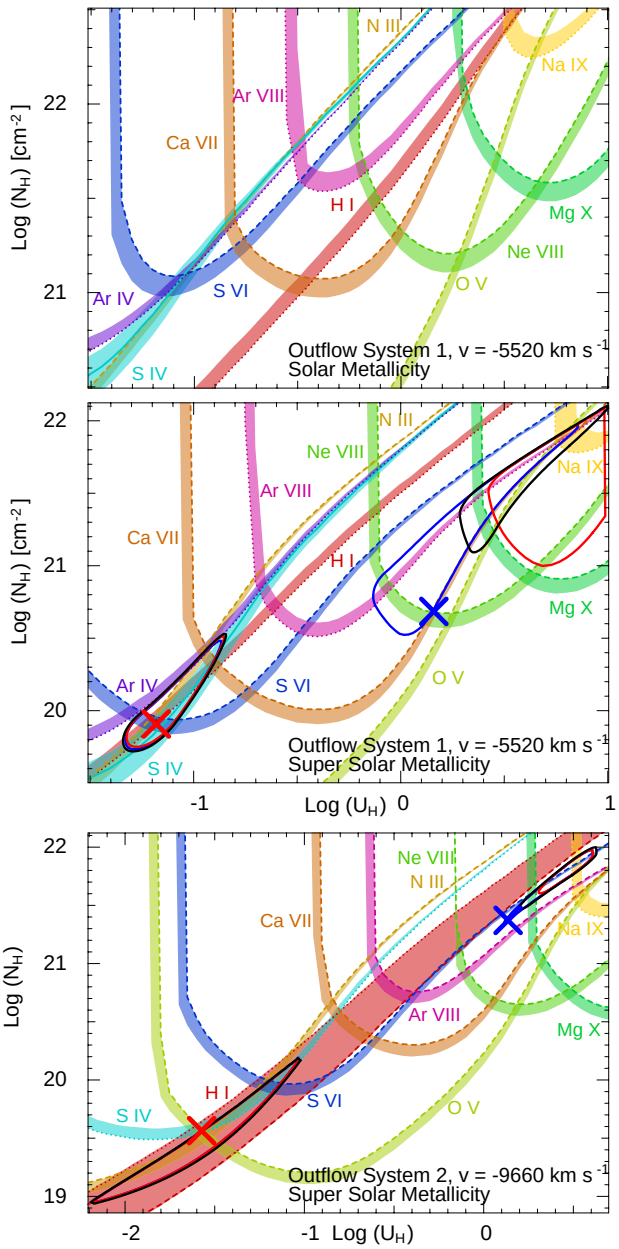

Figure 2. The best fitting photoionization solutions for outflows S1 and S2. **Top:** Comparison of the Cloudy modeled N$_{ion}$ to the measured N$_{ion}$ in S1 assuming solar metallicity. Each colored contour represents the region where the ($N_{\rm H}$, $U_{\rm H}$) model produces consistent N$_{ion}$ within the errors with the observed values. Solid lines represent N$_{ion}$ measurements while dotted and dashed lines represent upper and lower $N_{\rm ion}$ limits, respectively. Any solution that matches the upper limit N$_{ion}$ of H I underpredicts N$_{ion}$ of N III, S IV, and S VI by up to a factor of 5. **Middle and Bottom:** Under super-solar metallicity, the N$_{ion}$ from S1 and S2 match with two-phase photoionization solutions (see section 3.2). The very high- and high-ionization phase solutions are the blue and red "×" along with their 1σ error contours (the black ellipses), respectively. The black, blue, and red ellipses are accounting for the blending of troughs from Mg X λ624.94 and Ca VII λ624.38 (see section 3.2). The other $N_{\rm ion}$ lower and upper limits which are not shown here are consistent with the solutions and omitted for clarity's sake.

One possible solution is to invoke a super-solar metallicity. There were outflow systems which have been found to have super-solar metallicity (e.g., Gabel et al. 2006; Arav et al. 2007, 2019). In the middle and bottom panel of figure 2, we present the photoionization solutions assuming the HE0238 SED and the super-solar metallicity described in Paper V (Z = 4.68 $Z_{\odot}$). As in most of the other EUV500 outflows in our HST program GO-14777 (see table 1 of Paper I, except S4 in SDSS J1042+1646), we invoke a two-phase photoionization solution for both S1 and S2 (Arav et al. 2013). The very high-ionization phase (VHP) and high-ionization phase (HP) solutions are the blue and red "×" along with their 1σ error contours (the black ellipses), respectively. The ratios of the measured $N_{\rm ion}$ to the model predicted $N_{\rm ion}$ are given in the fourth column of table 2. When $N_{ion,mea}$ is a lower limit, we expect to have $N_{ion,mea}/N_{ion,model} < 1$ and vice versa.

Due to the blending absorption troughs from Mg X λ624.94 and Ca VII λ624.38 (S1 around 1135 Å and S2 around 1120 Å observed-frame, see figure 1), we present the photoionization solutions considering three different blending scenarios (figure 2). 1) half the trough's optical depth is from the Ca VIII ionic transition and the other half is from the Mg X ionic transition black ellipses), 2) the trough is comprised of only the ionic transition of Ca VII λ624.38 (blue ellipses), and 3) the trough is contributed from only the ionic transition of Mg X λ624.94 (red ellipses). For both S1 and S2, the blue "×" denotes the photoionization solution with the least $N_{\rm H}$ for the very high-ionization phase.

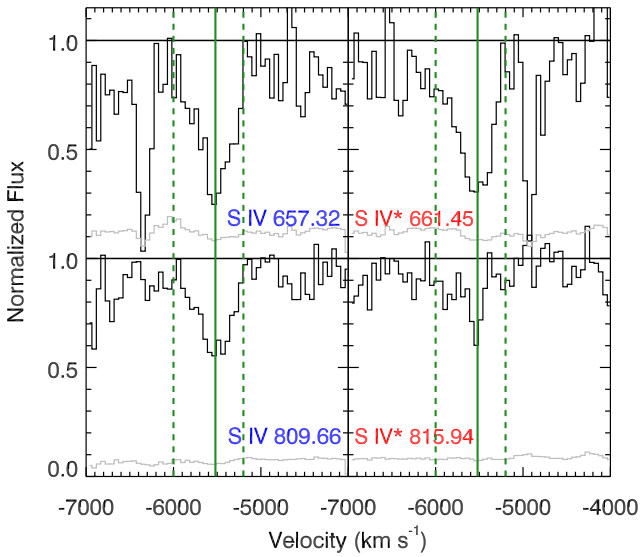

Figure 3. Comparison between two pairs of S IV and S IV* troughs for S1. The data are shown as the black histogram. The vertical, green solid line shows the velocity centroid of S1, while the $N_{\rm ion}$ integration range are shown as the dashed green lines (see section 4).

4. ELECTRON NUMBER DENSITY AND DISTANCES

By assuming the outflow is governed by photoionization, we can solve for R from equation (1). The only other unknown parameter is $n_{\rm H}$, and in a highly ionized plasma, $n_{\rm H} \approx 0.8 n_{\rm e}$. Here we use the density sensitive $N_{\rm ion}$ ratio from S IV*/S IV (for S1) and O III*/O III (for S2) to constrain $n_{\rm e}$.

Table 3
Atomic Data for S IV and S IV* Transitions

Ion	$\lambda^{(1)}$ (Å)	$E_{low}{}^{(2)}$ (cm^{-1})	$f^{(3)}$
S IV	657.319	0.00	1.130
S IV*	661.396	951.4	1.130
S IV	744.904	0.00	0.249
S IV	748.393	0.00	0.459
S IV*	750.221	951.4	0.597
S IV*	753.760	951.4	0.131
S IV	809.656	0.00	0.118
S IV*	815.941	951.4	0.085

Note. —
(1) Rest wavelength of S IV and S IV* transitions.
(2) Lower-level energy of these transitions from the National Institute of Standards and Technology (NIST) database (Kramida et al. 2018).
(3) Oscillator strengths from the NIST database.

4.1. *Determination of $n_{\rm e}$ for S1 from S IV*/S IV*

For S1, we observe absorption at the expected wavelength locations of the S IV lines listed in table 3. However, the 744.90 Å, 748.39 Å, 750.22 Å, and 753.76 Å troughs are severely blended with absorption troughs from S2 (see figure 1). Therefore, the $N_{\rm ion}$ from these S IV transitions can not be reliably determined. The 657.32 Å, 661.40 Å, 809.66 Å, and 815.94 Å troughs are not blended with other troughs from S2 or strong intervening systems (see figure 3). We show the comparison of these troughs in velocity space in figure 3.

The velocity centroids match well for these troughs as indicated by the green solid lines, while the $N_{\rm ion}$ integration ranges are the green dotted lines. The 815.94 Å trough clearly has less $N_{\rm ion}$ than the 809.66 Å trough, which is consistent with our derived N(S IV*)/N(S IV) ratio. For the AOD method, the expected optical depth (τ) ratio of the 657.32 Å trough to the 809.66 Å trough is:

$$\frac{\int \tau(v)_{657.32} dv}{\int \tau(v)_{809.66} dv} = \frac{N_{SIV} \times f_{657.32} \times 657.32}{N_{SIV} \times f_{809.66} \times 809.66} = 7.8 \quad (2)$$

where N(S IV) is the column density of S IV and $f_{657.32}/f_{809.66} \simeq 9.6$ is the oscillator strength ratio between the two transitions. By assuming that $\tau(v)_{657.32}/\tau(v)_{809.66}$ equals a constant, the expected ratio in the AOD case, i.e., $[\tau(v)_{657.32}/\tau(v)_{809.66}]_{\rm AOD}$, is 7.8. However, the observed ratio, i.e., $[\tau(v)_{657.32}/\tau(v)_{809.66}]_{\rm obs}$, is around 3, which indicates that the 657.3 Å trough is non-black saturated. Similarly, for the excited states of S IV, we derived $[\tau(v)_{661.40}/\tau(v)_{815.94}]_{\rm AOD} = 9.7$ and $[\tau(v)_{661.40}/\tau(v)_{815.94}]_{\rm obs} \simeq 3$. Therefore, the 661.40 Å trough is also non-black saturated. Thus, we use the PC method to obtain the $N_{\rm ion}$ for the S IV resonance state ($E_{\rm low} = 0\ {\rm cm}^{-1}$) from the 657.32 Å and 809.66 Å troughs and the excited state from the 661.40 Å and 815.94 Å troughs. The resulting ratio of the S IV* column density

to the S IV column density, i.e., N(S IV*)/N(S IV), is $0.54^{+0.20}_{-0.17}$.

In figure 4, we compare this S IV column density ratio to those predicted by the CHIANTI database (version 7.1.3, Landi et al. 2013). The mean temperature for S IV is 8700 K, which is based on the photoionization solution for the HP of S1 (section 3.2). The red curve is the model predictions from CHIANTI while the red cross is the derived N(S IV*)/N(S IV) ratio with its uncertainties. We find $\log(n_e) = 4.26^{+0.21}_{-0.20}$ (hereafter, n_e is in units of $\log(\mathrm{cm}^{-3})$).

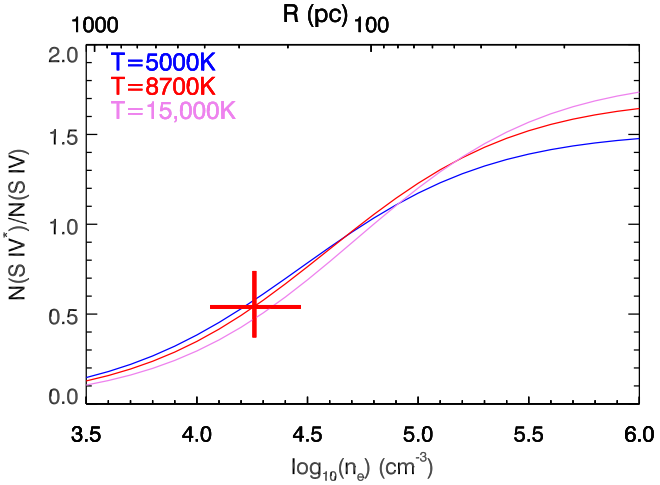

Figure 4. Column density ratio of S IV* to S IV vs. electron number density, n_e, for outflow S1. The red cross marks the ratio with the uncertainties derived in section 4. The colored curves are the predictions from the CHIANTI database (version 7.1.3, Landi et al. 2013) assuming different temperature. The mean temperature of the S IV gas based on the photoionization solution for the HP of S1 is 8700 K (section 3.2).

For outflow S1, we also observe absorption troughs from other density sensitive transitions, e.g., O IV λ787.71 and O IV* λ790.20 and O III+O III* near 833 Å in the observed frame (see figure 1). Unfortunately, their absorption troughs are either saturated or too blended to provide useful n_e constraints. However, their absorption troughs are consistent with our best fitting photoionization model. Therefore, by adopting the best-fit U_H and S IV-determined n_e into equation (1), we obtain $R = 270^{+100}_{-90}$ pc.

4.2. *Determination of n_e for S2 from O III*/O III*

For outflow S2, the stronger S IV and S IV* transitions at 657.32 Å and 661.40 Å do not show distinctive troughs. However, we detect deep absorption features at the expected wavelength location of the O III+O III* multiplet (O III λ832.93, and O III* $\lambda\lambda$833.75, 835.29). To determine n_e, we adopt the same analysis method from Paper II.

To fit the observed absorption features, we start with the photoionization solution inside the 1σ contour of the HP for S2 (the contour surrounding the red × in the bottom panel of figure 2). We vary $\log(n_e)$ from 2 to 8 and overlay the model predicted O III+O III* troughs to the

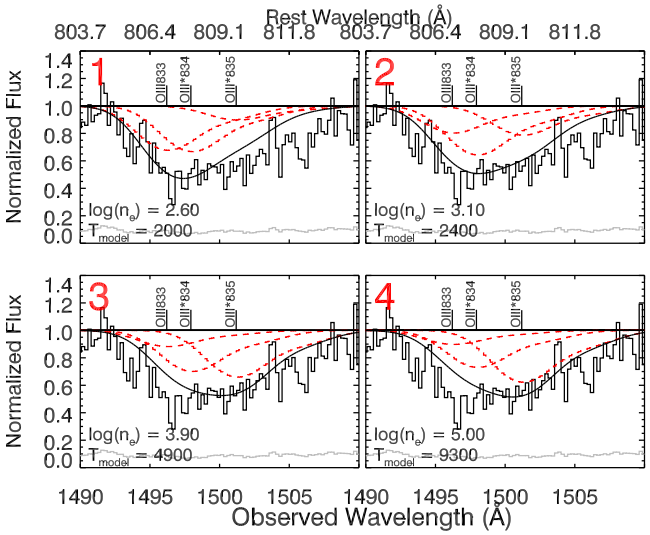

Figure 5. Fits to the O III+O III* multiplet region for outflow S2. To get the best fit, we vary n_e (in units of cm^{-3}) and probe the photoionization solution inside the 1σ error contour of the HP in S2. The n_e and the corresponding temperature predicted from Cloudy are shown at the bottom-left corner of each panel. The black and gray solid histograms are the normalized flux and errors from the HST/COS observations in 2017. For each subplot, the red dashed lines represent the models of the O III+O III* multiplet for a particular $\log(n_e)$, while the solid black lines are the summation of all models in this region. See section 4.2 for a detailed discussion.

1490 – 1510 Å observed-frame region (see figure 5). We then do a χ^2-minimization of the data and model for the O III+O III* region. The red dashed lines represent the modeled troughs of the O III+O III* multiplet for a particular n_e, while the solid black lines are the summation of all models in the region.

Since a single-Gaussian optical depth profile (e.g., equation (2) of Paper II) does not fit the O III+O III* region well, we adopt a two-Gaussian optical depth profile following Borguet et al. (2012b). The two Gaussians have the same velocity width (σ) of 350 km s^{-1}. The main Gaussian contains 65% of the total $N_{\rm ion}$ and has a velocity centroid (v_c) of –9660 km s^{-1}, while the secondary Gaussian contains 35% of the total $N_{\rm ion}$ with v_c = –8860 km s^{-1}. The same two-Gaussian profile also fits well the lower-velocity wing of other outflow troughs in S2, e.g., from Ar VIII λ713.80.

Adopting the two-Gaussian profile, the best-fitting $\log(n_e) = 3.1$, where the corresponding models are shown in the panel 2 of figure 5. The models with $\log(n_e) = 2.6$ and $\log(n_e) = 3.9$ deviate from the best-fitting model by 1σ (see panel 1 and 3 of figure 5), where they clearly underestimate the absorption troughs from 1500 – 1510 Å and 1493 – 1498 Å observed-frame, respectively. Overall, we get $\log(n_e) = 3.1^{+0.8}_{-0.5}$.

By adopting the best-fitting n_e value and errors into equation (1), we obtain $R = 1600^{+2000}_{-1100}$ pc.

5. OUTFLOW ENERGETICS

By assuming each outflow is in the form of a thin shell, covering a solid angle of $4\pi\Omega$ around the source, moving with a radial velocity v at a distance R from the central

Table 4
Physical Properties of the Outflow Systems Seen in Quasar SDSS J0755+2306

Outflow System	−5520 km s^{-1} (S1)		−9660 km s^{-1} (S2)	
Ionization Phase	Very High	High	Very High	High
$\log(N_{\rm H})$ [cm^{-2}]	> 20.7	$19.9^{+0.6}_{-0.2}$	21.4 – 22.0	$19.5^{+0.7}_{-0.6}$
$\log(U_{\rm H})$ [dex]	> 0.1	$-1.2^{+0.3}_{-0.2}$	0.1 – 0.6	$-1.6^{+0.6}_{-0.5}$
$\log(n_{\rm e})$ [cm^{-3}]	[a]<3.0	$4.3^{+0.2}_{-0.2}$	[a]<1.8	$3.1^{+0.8}_{-0.5}$
Distance [pc]	270^{+100}_{-90}		1600^{+2000}_{-1100}	
$\dot{M}$ [$M_\odot$ yr^{-1}]	> 20		450 – 8000	
$\log(\dot{E}_k)$[b] [erg s^{-1}]	>44.3		46.1 – 47.4	
$\dot{E}_k/L_{edd}$	>0.002		0.125 – 2.5	
$\log(f_{\rm V})$[c]	<-2.1		<-3.3	

Note. — Bolometric luminosity, $L_{\rm bol} = 4.4\times10^{46}$ erg s^{-1} assuming the HE0238 SED.
(a) Assuming that both ionization components are at the same distance.
(b) Assuming $\Omega = 0.2$ and where N_H is the sum of the two ionization phases.
(c) The volume filling factor of the outflow's high-ionization phase to the very high-ionization phase (see table 1 in Paper I and Arav et al. 2013).

source (see Paper I and Borguet et al. 2012a), the mass flow rate ($\dot{M}$) and kinetic luminosity ($\dot{E}_k$) of the outflow are given by:

$$\dot{M} \simeq 4\pi\Omega R N_{\rm H}\mu m_p v, \qquad \dot{E}_k \simeq \frac{1}{2}\dot{M}v^2 \tag{3}$$

where $N_{\rm H}$ is the total hydrogen column density, m_p is the proton mass, and $\mu = 1.4$ is the mean atomic mass per proton.

Using R with the $U_{\rm H}$ and $N_{\rm H}$ from the best-fitting photoionization solutions, we present the derived $\dot{M}$ and $\dot{E}_k$ values in table 4, where we assume $\Omega = 0.2$ (see section 6.4 of Paper II).

Using SDSS data, we measure the full-width-half-maximum of the Mg II broad emission line and estimate the Eddington luminosity (L_{edd}) with the Mg II–based black hole mass equation in Bahk et al. (2019). This leads to $L_{edd} = 1.0 \times 10^{47}$ erg s^{-1}. Therefore, outflows S1 and S2 yield the ratio of kinetic luminosity to L_{edd} of > 0.2% and 12 – 250%, respectively. The large range for S2 is due to the uncertainties of its $N_{\rm H}$ and $n_{\rm e}$, while the conservative lower limit of 12% is assured. Outflow S2, with $\dot{E}_k$ greater than 5% of L_{edd}, is a good candidate for producing strong AGN feedback (Scannapieco & Oh 2004).

6. DISCUSSION

6.1. *Partial Covering and Ionization State Relationship*

Outflows are found to only partially cover the emission source (e.g., Korista et al. 1992; Arav et al. 1999b, 2001, 2012; Hamann et al. 2001), and evidence exists to support the idea that the covering factor ($f_{\rm cov}$) becomes larger when the level of ionization within the outflow increases. For example, Korista et al. (1992) reported that the quasar 0226–1024 has an outflow with troughs from multiple doublet transitions arising from ions with different ionization potentials (IP). From the atomic data in Allen (1977), IP(O VI) = 77.41 eV > IP(C IV) = 64.49 eV > IP(Si IV) = 45.14 eV, and Korista et al. (1992) found that the depths of the saturated absorption troughs from these doublets follow the same trend. Possible explanations include that the outflows have small dense cores covered by loose envelopes. Therefore, the low-density envelopes with larger $f_{\rm cov}$ would tend to have higher-ionization levels than the high-density cores. However, elemental abundances are also found to affect the $f_{\rm cov}$ (Telfer et al. 1998; Arav et al. 1999a). Studying different ionization states from the same element eliminates the abundance effects and provide us with a direct test of the relationship between $f_{\rm cov}$ and ionization states.

Outflow S2 shows absorption troughs from two different ions of oxygen: the O III (IP = 55.9 eV) multiplet around 834 Å and the O VI (IP = 138.1 eV) doublet at 1031.93 Å and 1037.62 Å (see figure 1). From our photoionization solutions, the VHP produces a negligible amount of the $N_{\rm ion}$ for O III (< 0.1%) and almost ten times more $N_{\rm ion}$ for O VI than the HP. Therefore, O III and O VI are good candidates for testing the difference in f_{cov} between the phases. Our best fitting photoionization models predict that the absorption troughs from both of them are saturated, with $N_{model}/N_{mea} \sim 5$ and 30 for O III and O VI, respectively (see table 2). However, the O III doublet shows non-black saturation with residual flux ∼ 30 – 50%, while the O VI doublet has near zero residual flux (see figure 1). This directly supports the idea that for the same element, higher-ionization ions indeed cover a larger area of the emission source.

The O III and O VI troughs in S1 show a similar behavior and support the same idea, as the saturated O III multiplet in S1 shows residual flux ∼ 10% and the saturated O VI doublet has nearly zero residual flux.

6.2. *The λ > 1050 Å Portion of the Outflow Spectra*

Ground-based BAL quasar outflow (BALQSO) studies mainly cover the rest frame wavelength range of λ > 1050 Å, which usually show absorption troughs from only H I, N V, Si IV, and C IV. The widest trough with a measurable width for S1 is the O III multiplet near 820 Å (rest frame) with $\Delta v = 2500$ km s^{-1} (measured for continuous absorption below the normalized flux I = 0.9). For S2, we measure a width of 3100 km s^{-1} from the S VI 933.38 Å trough. Therefore, both of these outflows are identified as broad absorption line outflows (BALs, see section 6.3 of Paper II for elaboration).

From the best fitting photoionization solution derived in section 3.2, we can predict the absorption features for the λ > 1050 Å rest frame region for each outflow by assuming this region has the same absorption trough shape as in the EUV500 region. In figure 6, we show the predicted troughs. For outflows S1 and S2, the predicted C IV λλ1548.19, 1550.77 absorption troughs are saturated, blended, and have widths of 2400 km s^{-1} and 2600 km s^{-1}, respectively. Therefore, they are predicted to be BALs following the criteria of Weymann et al.

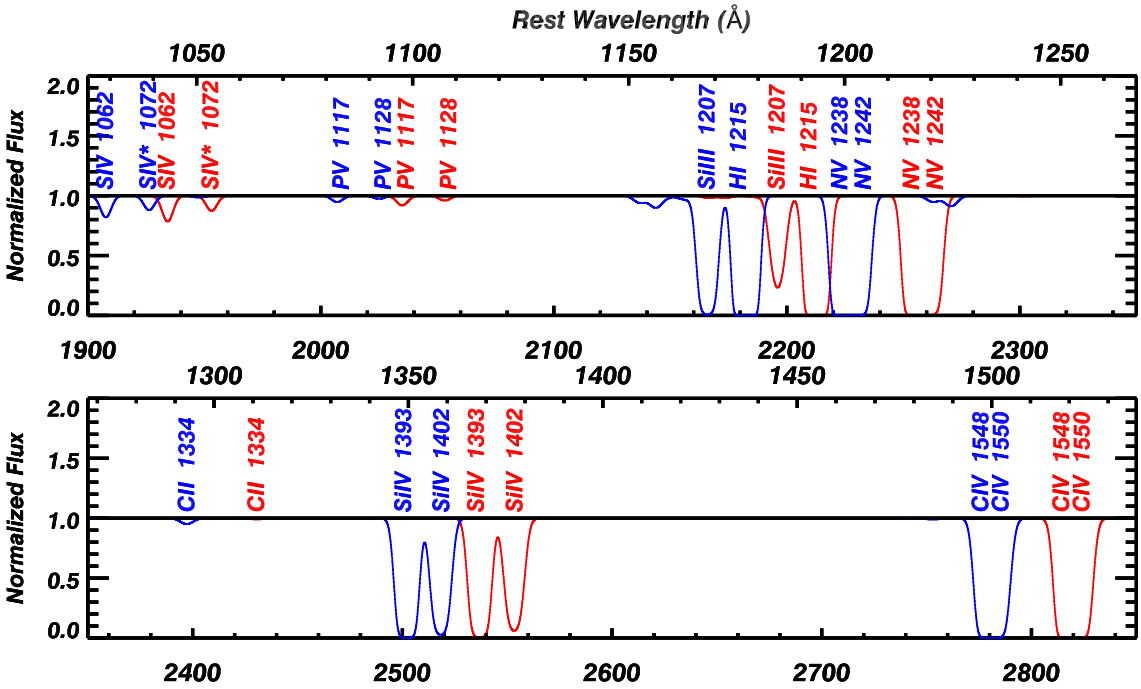

Figure 6. The predictions of the strong absorption troughs for outflows S1 and S2 in the $\lambda > 1050$ Å rest frame from the best fitting photoionization models (see section 3). The models for outflow S1 and S2 are shown in blue and red, respectively.

(1991).

The models also predict weak absorption troughs for both S IV λ1062.66 and S IV* λ1072.97 with oscillator strengths (f) for both about 0.05, which are the main density sensitive transitions for the $\lambda > 1050$ Å rest frame region (Arav et al. 2018). However, the predicted troughs have maximum optical depths around 0.05, which make their detection unlikely with ground-based telescopes for a couple of reasons. First, $\tau = 0.05$ troughs are difficult to detect in principle due to their shallowness and systematic issues regarding the unabsorbed emission model. Second and more important, from the ground we can detect the 1062 Å rest-frame wavelength region only for quasars with redshifts $z \gtrsim 2.5$. At these redshifts, the Lyα forest severely contaminates the S IV troughs, which makes the task of identifying such shallow trough hopeless in SDSS data and very difficult in Very Large Telescope (VLT)/X-shooter observations (the latter observations have both higher S/N and spectral resolution than the SDSS data, see Arav et al. 2018; Xu et al. 2018, 2019).

In contrast, for the same outflow, we have four detected pairs of S IV and S IV* troughs in the EUV500 with associated f values up to 20 times larger (resulting in deeper troughs for the same amount of S IV N_{ion}). Also the availability of two uncontaminated pairs of S IV and S IV* troughs in S1, with large f value differences, makes the n_e determination more robust and less affected by possible systematic issues. Based on these S IV and S IV* EUV500 troughs, we were able to determine the n_e, R, and energetics for outflow S1 (see section 4).

We also note that the predicted P V troughs are even shallower than the S IV λ1062.66 and S IV* λ1072.97 ones, which explains the low detection rate of P V troughs among BAL quasars (3.0 – 6.2%, see Capellupo et al. 2017).

7. SUMMARY

In this paper, we analyzed outflows seen in the recent HST/COS spectra of quasar SDSS J0755+2306. The main results are summarized as follows:

1. Two outflow systems are identified. They present clear absorption troughs from both high-ionization species, e.g., N III, O III, O IV and S IV, and very high-ionization species, e.g., Ar VIII, Ne VIII, and Na IX (see section 2). Both outflows are classified as BALs from their widest EUV500 absorption trough widths.
2. Similar to the outflow analysis in Papers II, III, and V, each outflow system requires a two ionization-phase solution (see section 3.2).
3. For outflow system 2, we derive $\log(n_e) = 3.1$ based on the density sensitive transitions of O III and O III* in the EUV500 band. The determined distance of this outflow is 1600 pc and the kinetic luminosity is >12% of L_{edd} (see section 4 and 5). Therefore, this outflow is a good candidate for producing strong AGN feedback.
4. The absorption troughs from O III and O VI support the idea that high-ionization ions have a larger covering fraction compared to lower-ionization ions (see section 6.1).

X.X., N.A., and T.M acknowledge support from NSF grant AST 1413319, as well as NASA STScI grants GO 11686, 12022, 14242, 14054, 14176, and 14777, and NASA ADAP 48020.

Based on observations made with the NASA/ESA Hubble Space Telescope, obtained from the data archive at the Space Telescope Science Institute. STScI is operated by the Association of Universities for Research in Astronomy, Inc. under NASA contract NAS 5-26555.

CHIANTI is a collaborative project involving George Mason University, the University of Michigan (USA) and the University of Cambridge (UK).

REFERENCES

Allen, K. W. 1977, Astrophysical quantities., by Allen, K. W.. Translated from the 3. revised and suppl. English edition. Moskva: Mir, 448 p.,

Arav, N., Korista, K. T., de Kool, M., Junkkarinen, V. T., & Begelman, M. C. 1999, ApJ, 516, 27

Arav N., Becker R. H., Laurent-Muehleisen S. A., Gregg M. D., White R. L., Brotherton M. S., de Kool M., 1999, ApJ, 524, 566

Arav, N., de Kool, M., Korista, K. T., et al. 2001, ApJ, 561, 118

Arav, N., Gabel, J. R., Korista, K. T., et al. 2007, ApJ, 658, 829

Arav, N., Edmonds, D., Borguet, B., et al. 2012, A&A, 544, AA33

Arav, N., Borguet, B., Chamberlain, C., Edmonds, D., & Danforth, C. 2013, MNRAS, 436, 3286

Arav, N., Liu, G., Xu, X., et al. 2018, ApJ, 857, 60

Arav, N., Xu, X., Kriss, G. A., et al. 2019, submitted to ApJ

Arav, N., Xu, X., Miller, T. R., et al. 2020, ApJS, in press

Bahk, H., Woo, J.-H., & Park, D. 2019, ApJ, 875, 50

Borguet, B. C. J., Edmonds, D., Arav, N., Dunn, J., & Kriss, G. A. 2012a, ApJ, 751, 107

Borguet, B. C. J., Edmonds, D., Arav, N., Benn, C., & Chamberlain, C. 2012, ApJ, 758, 69

Chamberlain, C., Arav, N., & Benn, C. 2015, MNRAS, 450, 1085

Choi, E., Naab, T., Ostriker, J. P., Johansson, P. H., & Moster, B. P. 2014, MNRAS, 442, 440

Ciotti, L., Ostriker, J. P., & Proga, D. 2009, ApJ, 699, 89

Capellupo, D. M., Hamann, F., Herbst, H., et al. 2017, MNRAS, 469, 323

Ferland, G. J., Chatzikos, M., Guzmn, F., et al. 2017, RMxAA, 53, 385

Gabel, J. R., Arav, N., & Kim, T.-S. 2006, ApJ, 646, 742

Ganguly, R., & Brotherton, M. S. 2008, ApJ, 672, 102-107

Gibson, R. R., Jiang, L., Brandt, W. N., et al. 2009, ApJ, 692, 758

Green J. C., et al., 2012, ApJ, 744, 60

Hamann, F. W., Barlow, T. A., Chaffee, F. C., Foltz, C. B., & Weymann, R. J. 2001, ApJ, 550, 142

Hewett P. C., Foltz C. B., 2003, AJ, 125, 1784

Hopkins, P. F., & Elvis, M. 2010, MNRAS, 401, 7

Hopkins, P. F., Torrey, P., Faucher-Giguère, C.-A., Quataert, E., & Murray, N. 2016, MNRAS, 458, 816

Korista, K. T., Weymann, R. J., Morris, S. L., et al. 1992, ApJ, 401, 529

Landi, E., Young, P. R., Dere, K. P., Del Zanna, G., & Mason, H. E. 2013, ApJ, 763, 86

Miller, T. R., Arav, N., Xu, X., et al. 2018, ApJ, 865, 90

Miller, T. R., Arav, N., Xu, X., et al. 2020, ApJS, in press

Miller, T. R., Arav, N., Xu, X., et al. 2020, ApJS, in press

Miller, T. R., Arav, N., Xu, X., et al. 2020, in preparation

Kramida, A., Ralchenko, Yu., Reader, J., and NIST ASD Team (2018). NIST Atomic Spectra Database (ver. 5.6.1), [Online]. Available: https://physics.nist.gov/asd [2019, April 26]. National Institute of Standards and Technology, Gaithersburg, MD. DOI: https://doi.org/10.18434/T4W30F

Ostriker, J. P., Choi, E., Ciotti, L., Novak, G. S., & Proga, D. 2010, ApJ, 722, 642

Prochaska, J. X., Herbert-Fort, S., & Wolfe, A. M. 2005, ApJ, 635, 123

Reichard, T. A., Richards, G. T., Schneider, D. P., et al. 2003, AJ, 125, 1711

Scannapieco, E., & Oh, S. P. 2004, ApJ, 608, 62

Schlafly, E. F., & Finkbeiner, D. P. 2011, ApJ, 737, 103

Trump, J. R., Hall, P. B., Reichard, T. A., et al. 2006, ApJS, 165, 1

Telfer, R. C., Kriss, G. A., Zheng, W., Davidsen, A. F., & Green, R. F. 1998, ApJ, 509, 132

Tolea, A., Krolik, J. H., & Tsvetanov, Z. 2002, ApJ, 578, L31

Weymann, R. J., Morris, S. L., Foltz, C. B., & Hewett, P. C. 1991, ApJ, 373, 23

Wright, E. L. 2006, PASP, 118, 1711

Xu, X., Arav, N., Miller, T., & Benn, C. 2018, ApJ, 858, 39

Xu X., Arav N., Miller T., Benn C., 2019, ApJ, 876, 105

Xu, X., Arav, N., & Miller, T. 2020, ApJS, in press

Xu, X., Arav, N., & Miller, T. 2020, ApJS, in press

Xu, X., Arav, N., & Miller, T. 2020, ApJS, in press